



Cite this: *Nanoscale*, 2017, 9, 14236

A bifunctional nanomodulator for boosting CpG-mediated cancer immunotherapy†

 Zhenzhen Wang,^{a,b} Yan Zhang,^{a,b} Zhen Liu,^a Kai Dong,^a Chaoqun Liu,^{a,b} Xiang Ran,^{a,b} Fang Pu,^a Enguo Ju,^{a,b} Jinsong Ren ^{*a} and Xiaogang Qu ^{*a}

Unmethylated cytosine-phosphate-guanine (CpG) oligonucleotides (ODNs) possess high immunostimulatory activity and represent attractive tools for cancer treatment. However, their success in eliminating large solid tumors was hampered by the immunosuppressive tumor microenvironment. Herein, we report that the design of a novel MnO₂–CpG–silver nanoclusters (AgNCs)–doxorubicin (DOX) conjugate for enhanced cancer immunotherapy, in which MnO₂ nanosheets function as unique supports to integrate the chemotherapy drug DOX and the immunotherapeutic agent CpG–AgNCs. Importantly, DOX could be conjugated with MnO₂ nanosheets through π – π interactions to serve as a bifunctional modulator of the tumor microenvironment to activate a tumor-specific immune response by inducing immunogenic cell death, and reverse the immunosuppressive tumor microenvironment *via* abrogating the immune-suppressive activity of regulatory T cells, both of which would greatly improve the immune response of CpG–AgNCs. In this way, the T-cell immune responses of CpG–AgNCs which are linked to MnO₂ nanosheets were significantly enhanced and could exhibit remarkable antitumor activity against large solid tumors. Our study may guide the rational design of immunotherapeutic boosters for improving cancer treatment.

 Received 19th June 2017,
 Accepted 23rd August 2017

DOI: 10.1039/c7nr04396a

rsc.li/nanoscale

Introduction

As a type of immunostimulatory nucleic acid, unmethylated cytosine-phosphate-guanine (CpG) oligonucleotides (ODNs) have attracted increasing attention due to their strong immunostimulating activity.^{1–4} The recognition of CpG ODNs by Toll-like 9 (TLR9) of the host cell could induce a cascade of innate and adaptive immune responses *via* the MyD88-dependent nuclear factor- κ B (NF- κ B) and mitogen-activated protein kinase (MAPK) signaling pathways, promoting the secretion of proinflammatory cytokines such as IL-12, IL-6, TNF- α , IFN- γ *etc.*^{5–7} Such properties make CpG ODNs promising therapeutic candidates for treating cancer. Particularly, clinical trials of CpG ODNs have been conducted from phase I to III and shown some exciting results.^{8–12} Nevertheless, owing to the strong immunosuppressive effect of the tumor microenvironment, a high dose of CpG ODNs and repetitive administration were required to obtain an effective immune effect, which led to adverse effects (*e.g.* sepsis-like events).^{13–15}

Furthermore, CpG ODN monotherapy was efficient against tumors only with a small size (<20 mm³) rather than large solid tumors as advanced tumors were more immunosuppressive.^{16–19} These limitations greatly hampered their further application in the clinic. To tackle these challenges, therapeutic interventions aimed at disrupting the immunosuppressive mechanisms of tumors have emerged as promising strategies to enhance the antitumor immunity of CpG ODNs.^{20–22} In particular, immune checkpoint blockade therapy that uses small-molecule inhibitors or antibodies to suppress regulatory pathways in T cells could promote the immune responses of CpG-ODNs significantly and thereby inhibit tumor growth.^{23,24} However, the limited efficacy and the non-specific immunological response of checkpoint blockade therapy would lead to severe side effects, including autoimmune disorders, and hepatic and endocrinological toxicities, which retarded their clinical translation.^{25–27} Thus, it is highly necessary to develop a new paradigm that could improve the therapeutic effects of CpG ODNs effectively to treat large solid tumors while avoiding the untoward side effects.

Chemotherapy is the gold-standard treatment modality for cancer.^{28,29} Since most chemotherapeutics killed tumor cells through cytostatic and/or cytotoxic effects, the contribution of chemotherapy to the immune system has long been neglected.^{30–32} Recently, accumulating evidence suggests that

^aLaboratory of Chemical Biology and State Key Laboratory of Rare Earth Resources Utilization, Changchun Institute of Applied Chemistry, Chinese Academy of Science, Changchun, Jilin 130022, China. E-mail: jren@ciac.ac.cn, xqu@ciac.ac.cn

^bUniversity of Chinese Academy of Sciences, Beijing 100039, China

†Electronic supplementary information (ESI) available. See DOI: 10.1039/c7nr04396a

certain chemotherapeutic agents can modify the propensity of tumor cells to elicit an immune response and/or directly exert immunostimulatory effects.^{33–36} Among them, doxorubicin (DOX), a commonly used anticancer agent in the clinic, has been demonstrated to be an impactful agent of both the innate and the adaptive immune response.^{37,38} On the one hand, DOX could engage a tumor-specific immune response by eliciting immunogenic cell death (ICD), where the dying tumor cells acting as anticancer vaccines initiated a robust immune response.^{39–42} Such effects not only promoted the antigen-presenting capacity of antigen-presenting cells, but also stimulated the secretion of pro-inflammatory cytokine. More importantly, recent research has demonstrated that immunocompetent mice vaccinated with dying cancer cells which were pre-treated with DOX were protected against subsequent challenges with live cancer cells.⁴³ In addition, DOX has the potential to alter tumor microenvironments to decrease immune suppression by abrogating the immune-suppressive activity of regulatory T cells (Tregs) and improving the activities of effector T-cells, which are crucial for reopening the dormant immune response against malignancies.^{44–46} By taking these unique advantages of immunogenic drugs, we envision that DOX would augment the immune response of CpG and enhance its antitumor efficiency for large solid tumors.

Herein, for the first time, we reported that the construction of MnO₂-CpG-silver nanocluster (AgNCs)-DOX (MCAD) nanocomposites could realize a highly effective cancer immunotherapy, in which MnO₂ nanosheets functioned as a unique support to integrate DOX and CpG-AgNCs together (Fig. 1A). DOX was conjugated with MnO₂ nanosheets through π - π interactions to behave as a bifunctional modulator that was capable of inducing ICD and decreasing the immunosuppressive tumor microenvironment to boost CpG-mediated cancer immunotherapy. In this way, the antitumor immunity of CpG-AgNCs which could link to MnO₂ nanosheets through physisorption was significantly enhanced. As illustrated in Fig. 1B, upon MCAD nanocomposite internalization into tumor cells, DOX-attenuated tumor cells emitted three distinct “danger” signals, namely calreticulin (CRT) exposure, ATP secretion, and the extracellular nuclear high-mobility group box 1 protein (HMGB1) release, which were recognized by the immune system.^{47,48} These signals were then processed and presented by infiltrated antigen-presenting cells and thereby stimulated a strong tumor-specific immune response. More importantly, DOX had a similar effect as immune checkpoint blockade therapy that inhibited the immune-suppressive activity of Tregs and improved the activities of effector T-cells.⁴⁴ Such a bifunctional immune effect of DOX made it possible to overcome the shortcomings of CpG-AgNCs *in vivo*. For the first time, we found that with the assistance of DOX, CpG-AgNCs not only induced immune activity significantly *in vivo* but also eradicated the large solid tumors effectively. This new finding may open the way to the application of chemotherapeutic drugs as immunotherapeutic boosters to complement current treatment paradigms for treating many difficult-to-treat cancers. In addition, benefiting from the fluo-

rescence properties of CpG-AgNCs and the excellent T₁-magnetic response imaging (MRI) performance of Mn²⁺, our MCAD nanocomposites successfully realized tumor-activatable MRI and fluorescence imaging *in vivo*, providing a comprehensive and efficient tool for real-time tracking of the CpG release and evaluating the treatment efficacy.

Experimental

Materials

Manganese chloride tetrahydrate (MnCl₂·4H₂O) and tetramethylammonium hydroxide were obtained from Aladdin. H₂O₂ was obtained from Beijing Chemicals (Beijing, China). Silver nitrate (AgNO₃, 99.9995%) and sodium borohydride (NaBH₄, 98%) were bought from Alfa Aesar. All chemicals were utilized as received from the suppliers without further purification. Of note, we used ultrapure water (18.2 M Ω ; Millipore Co., USA) throughout the experiment. DNA oligonucleotides were prepared by Shanghai Sangon Biological Engineering Technology & Services (Shanghai, China). The sequences were as follows: CpG (1826) oligodeoxynucleotides: 5'-TCC ATG ACG TTC CTG ACG TT-3'; DNA template for CpG-AgNC (CpG-AgNCs): 5'-TCC ATG ACG TTC CTG ACG TTA AAA AAA AAA CCC CCC CCC CCC-3'. Purified anti-mouse TNF- α , biotin conjugated anti-mouse TNF- α , TNF- α standard, purified anti-mouse IFN- γ , biotin conjugated anti-mouse IFN- γ and IFN- γ standards were bought from eBioscience. Anti-CD3e-APC, anti-CD4-FITC and anti-CD8a-FITC were purchased from Biolegend.

Measurements and characterization

Fluorescence measurements were recorded using a JASCO FP-6500 spectrofluorometer (Jasco International Co., Japan). Transmission electron microscopy (TEM) images were carried out by using a FEI TECNAI G2 20 high-resolution transmission electron microscope operating at 200 kV. Ultraviolet-visible (UV-Vis) spectra were recorded on a JASCO-V550 spectrometer. XPS measurements were recorded with an ESCALAB-MKII spectrometer (VG Co., United Kingdom) with Al K α X-ray radiation as the X-ray source for excitation.

Preparation of MnO₂ nanosheets

MnO₂ nanosheets were synthesized according to previous reports with a slight modification.⁴⁹ Briefly, 0.6 M tetramethylammonium hydroxide and 3 wt% H₂O₂ were simultaneously added into MnCl₂ solution (10 mL, 0.3 M). The mixture became dark brown immediately, showing that Mn²⁺ ions were oxidized into Mn⁴⁺. Then, the mixture was collected by centrifugation and washed three times with distilled water. To obtain the MnO₂ nanosheets, 25 mg bulk MnO₂ was dissolved in 50 mL water and sonicated for 10 h. Finally, the dispersion was centrifuged at 5000 rpm, and the supernatant was MnO₂ nanosheets.

Synthesis of CpG-AgNCs

AgNCs were prepared by cooling the mixture of DNA and AgNO₃ to 0 °C, followed by adding fresh NaBH₄ solution, and

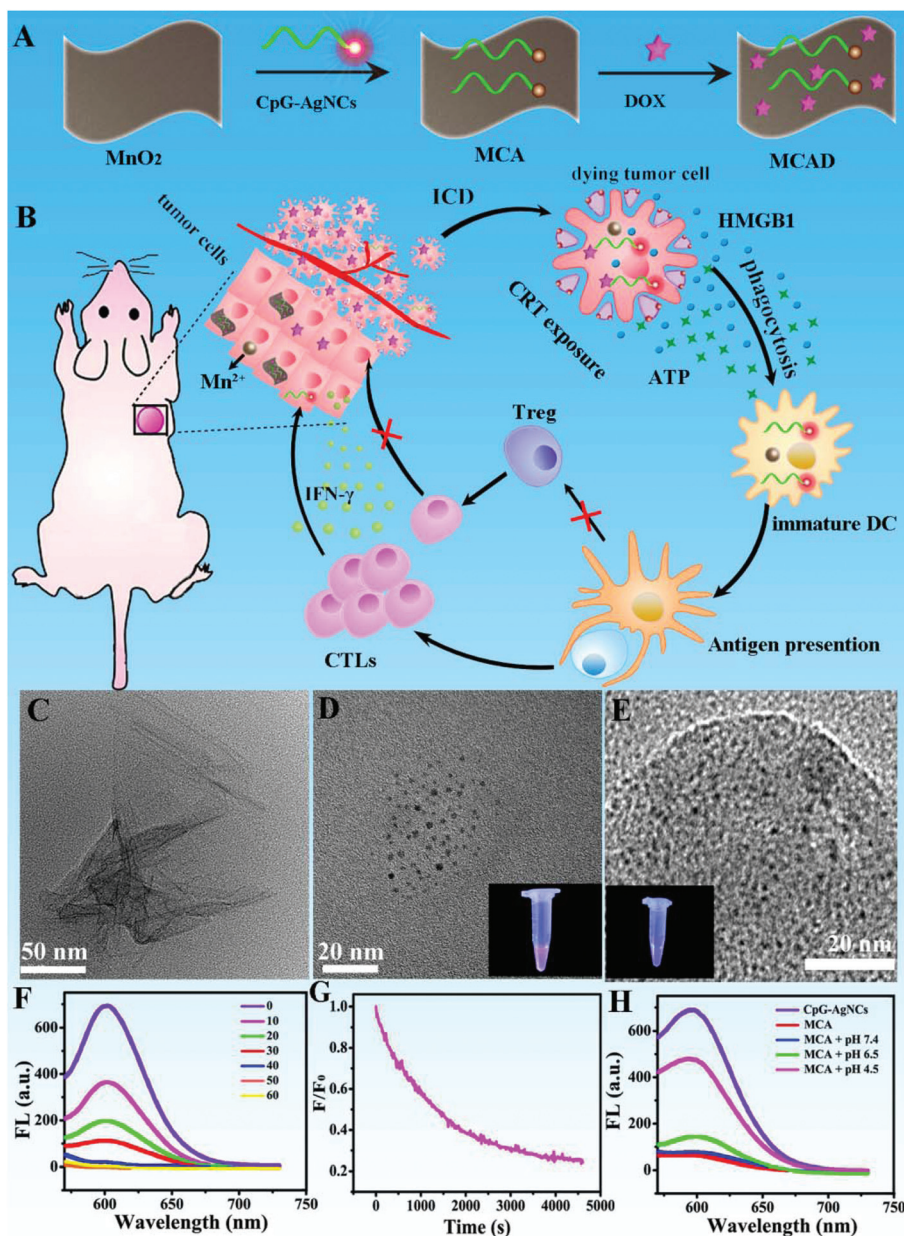


Fig. 1 (A) Schematic illustration of the synthetic procedure for MCAD nanocomposites. (B) The mechanism of anti-tumor immune responses induced by MCAD nanocomposites. (C)–(E) TEM characterization studies of MnO_2 nanosheets, CpG-AgNCs nanoparticles and MCA nanocomposites, respectively. (F) The fluorescence of CpG-AgNCs on the surface of MnO_2 nanosheets at different concentrations. (G) Kinetics study of the fluorescence change at 600 nm of the CpG-AgNCs in the presence of MnO_2 nanosheets. (H) The fluorescence recovery of CpG-AgNCs in a mimicking tumor microenvironment, where exists an acidic H_2O_2 microenvironment.

then the mixture was acutely shaken for 2 min. The final concentrations were 10 μM for DNA, 60 μM for AgNO_3 , and 60 μM for NaBH_4 . Unless otherwise noted, experiments were performed in 25 mM phosphate buffer saline (PBS) at pH 7.4. Then, the fluorescence stability of CpG-AgNCs in different pH values was investigated.

Synthesis of MCA nanocomposites

The physisorption of CpG-AgNCs on MnO_2 nanosheets (MCA) was carried out by mixing 20 μL of MnO_2 nanosheets

(200 mg L^{-1}) and 10 μL CpG-AgNCs (10 μM) for 10 minutes and then adding 70 μL of HEPES buffer for further incubation for 20 min. Then, the fluorescence measurements of MCA and equivalent CpG-AgNCs were performed.

Synthesis of MnO_2 -DOX and MCAD nanocomposites

MnO_2 nanosheets were added to 20 mL of a 0.5 mg mL^{-1} DOX solution, and then the mixture was stirred for 4 h at 25 $^\circ\text{C}$. The MnO_2 -DOX nanocomposites were obtained by centrifugation, and then were further dispersed into PBS solution. The

loading amount of DOX was detected by a UV-Vis test ($\lambda = 480$ nm) of the initial DOX solution and the supernatant DOX after centrifugation. Similarly, the MCAD nanocomplex was prepared according to the above method. The MCA solution was mixed with DOX for 4 h at 25 °C, and the mixture was centrifuged to remove excess DOX.

Cell culture

Both RAW264.7 cells and 4T1 cells were supplied by the ATCC (American Type Culture Collection). The RAW264.7 cells and 4T1 cells were incubated with Dulbecco's modified Eagle's medium (DMEM) containing 10% heat-inactivated fetal bovine serum (FBS) at 37 °C under an atmosphere of 5% (v/v) CO₂ in the air. The medium was replaced every two days. The cells were digested using trypsin and redispersed in a fresh medium before plating.

In vitro phagocytosis assay

4T1 cells were labeled with 1 μ M CellTracker Orange (Sigma-Aldrich) were transferred to a 1.5 mL Eppendorf microtube and treated with PBS, MnO₂ nanosheets (50 μ g mL⁻¹), DOX (3 μ M) or MnO₂-DOX (with a DOX concentration of 3 μ M) for 4 h in an Eppendorf shaker at 37 °C. 4 h later, 4T1 cells were co-cultured with Raw264.7 cells which were pre-seeded into 24-well plates for 24 h and then labeled with 1 μ M CellTracker Green (Sigma-Aldrich) at a 1:10 ratio for 2 h. To prevent the nonspecific absorption of 4T1 cells on the surface of RAW264.7 cells, the wells were washed with PBS three times before fluorescence analysis.

CRT exposure

The CRT exposure induced by DOX was assessed by immunofluorescence and flow cytometry. To conduct immunofluorescence experiments, 4T1 cells (5 \times 10⁴ per well) were seeded into 24-well plates and maintained for 24 h. Then, the 4T1 cells were incubated with free DOX or MnO₂-DOX nanocomposites at an equivalent DOX dose of 3 μ M. 4T1 cells treated with PBS functioned as a control. After 4 h incubation, the cells were cultured with an Alexa Fluor 488-CRT antibody for an additional 2 h and observed by fluorescence microscopy. Additionally, the CRT exposure induced by DOX was analyzed by flow cytometry. 4T1 cells were seeded into 6-well plates at a density of 1 \times 10⁶ cells per well and maintained for 24 h. After 4 h incubation, the cells were treated with an Alexa Fluor 488-CRT antibody for 2 h and then stained with PI. Flow cytometric analysis was performed to identify cell surface CRT by gating on PI-negative cells.

ATP secretion assay

4T1 cells (1 \times 10⁶ per well) were seeded into 6-well plates in DMEM medium. The next day, cells were incubated with different groups including PBS, MnO₂ nanosheets (50 μ g mL⁻¹), DOX (3 μ M) or MnO₂-DOX (with a DOX concentration of 3 μ M) for 24 h and the conditioned supernatant was carefully collected for extracellular ATP measurements by using a luciferin-based ENLITEN ATP Assay kit.

Flow cytometric analysis of HMGB1 release

4T1 cells (1 \times 10⁶ per well) in 6-well plates were treated with PBS, MnO₂ nanosheets (50 μ g mL⁻¹), DOX (3 μ M) or MnO₂-DOX (with a DOX concentration of 3 μ M) for 24 h and washed several times with PBS. Then, the cells were fixed, permeabilized and stained with FITC-conjugated anti-HMGB1 for 30 min, and observed by flow cytometry.

Anti-proliferative activity of MCAD on 4T1 co-incubated with RAW264.7 cells

Transwell plate assay was conducted to assess the anti-tumour effect of our system. Briefly, 4 \times 10⁴ cells RAW264.7 per well and 4 \times 10³ 4T1 cells were added to the upper and lower chambers, respectively. MnO₂ nanosheets (50 μ g mL⁻¹), free CpG ODNs (5 μ M), MnO₂-DOX (with a DOX concentration of 3 μ M), MCA (with a CpG concentration of 5 μ M) and MCAD nanocomposites (with a CpG concentration of 5 μ M and a DOX concentration of 3 μ M) were added to the upper side, respectively. Following incubation for 48 h, the proliferative ability of 4T1 cells in the lower chambers was determined by MTT assay.

Cytokine assays

1 \times 10⁶ RAW264.7 cells per cell were seeded on 6-well culture plates. After incubation for 24 h, cells were incubated with the indicated conditions for 24 h (IL-6) or 8 h (TNF- α). The conditioned media was carefully extracted and stored at -80 °C until use. The concentrations of IL-6 and TNF- α were evaluated by enzyme-linked immunosorbent assay (ELISA).

In vivo tumor models

We purchased 8-week-old female Balb/c mice from the Laboratory Animal Center of Jilin University (Changchun, China). Notably, all animal procedures were in accord with the guidelines of the Institutional Animal Care and Use Committee. To develop a tumor model, 4T1 cells (1 \times 10⁶) dispersed in PBS were subcutaneously injected into the flank mammary gland of each female Balb/c mouse. When the tumor volume reached \approx 100 mm³, mice were divided into four groups including PBS (control), MCA (immunotherapy), MnO₂-DOX (chemotherapy) and MCAD (synergistic therapy), where each group consisted of 5 mice and was administered doses by intratumoral injection. The concentration and dose used for the four groups are shown in Table 1. It deserves mentioning that the tumor volume was calculated according to the following formula: Volume = (Tumor Length) \times (Tumor Width)²/2.

Table 1 The concentration used of four groups

PBS	MCA	MnO ₂ -DOX	MCAD
50 μ L 10 mM	50 μ L CpG 5 μ M	50 μ L DOX 2 mg mL ⁻¹	50 μ L CpG 5 μ M DOX 2 mg mL ⁻¹

Levels of IFN- γ

In order to study the *in vivo* immune response of MCAD, a particular soluble cytokine IFN- γ was evaluated. The tumor-bearing mice received intratumoral injections of PBS, MCA (with a CpG concentration of 5 μ M), MnO₂-DOX (with a DOX concentration of 2 mg mL⁻¹), MCAD (with a CpG concentration of 5 μ M and a DOX concentration of 2 mg mL⁻¹). After 3 days of treatment, the serum samples of mice in each group were collected and diluted for analysis. The levels of IFN- γ in the sera were determined by ELISA using antibody pairs specific to the cytokine following the manufacturer's instructions.

Flow cytometry (FACS) assay of cell surface markers

Tumors were harvested, incubated with 1 mg mL⁻¹ collagenase I for 1 h and ground with the rubber end of a syringe. Then, cells were filtered by nylon mesh filters and washed several times with PBS. The obtained single-cell suspension was treated with anti-CD3e-APC and anti-CD4-FITC or anti-CD8a-FITC. FACS analysis was used to analyse the stained cells. Intracellular FoxP3 staining was performed by using a T Cell Staining kit.

Statistical analysis

All data were presented in this work as the mean \pm standard deviation (SD). All figures exhibited in this work were acquired from three independent experiments with similar results. The statistical analysis was conducted by using Origin 8.0 software. Asterisks indicate significant differences (* P < 0.05, ** P < 0.01, *** P < 0.001).

Results and discussion

Characterization of MCAD nanocomplexes

To verify our hypothesis, the CpG-AgNCs nanoparticles were initially synthesized by silver metallization of CpG DNA containing a 12-base C-nucleation sequence.⁵⁰ Transmission electron microscopy (TEM) and HRTEM images of CpG-AgNCs demonstrated their size of about 2 nm with good uniformity (Fig. 1D, Fig. S1 and S2†). Moreover, the well-prepared CpG-AgNC nanoparticles exhibited bright red fluorescence with an excitation wavelength of 550 nm and an emission wavelength of 600 nm, which were favorable for investigating the dynamic processes of CpG-AgNCs *in vivo* (Fig. S3†). Importantly, no significant photobleaching was detected over a broad pH range, indicating the good fluorescence stability of CpG-AgNCs in various acidic/basic media (Fig. S4†). Furthermore, we found that the introduction of AgNCs greatly increased CpG stability against nuclease degradation (Fig. S5†), which was helpful for their applications *in vivo*. Owing to their appealing pH-/redox-responsive properties, abundant anchoring points and extremely large surface area, MnO₂ nanosheets were specifically chosen as nanocarriers in our work.⁵¹ The MnO₂ nanosheets were prepared according to a previous report⁴⁹ and had an average size of 223 nm as well as a polycrystalline sheet structure determined by TEM and dynamic light scattering (Fig. 1C, Fig. S6 and S7†). Atomic force microscopy (AFM) imaging

showed the typical two-dimensional appearance of MnO₂ with a thickness of 1.1 nm (Fig. S8†).

Of note, single-stranded DNA could be absorbed on the surface of MnO₂ nanosheets by the synergistic physisorption of nucleobases on the basal plane of the MnO₂ nanosheets.⁴⁹ Encouraged by this property, we investigated whether the flexible single strand state of CpG-AgNCs was capable of absorbing on the surface of MnO₂ nanosheets. As revealed by TEM images, CpG-AgNC nanoparticles were successfully dispersed on the surface of MnO₂ nanosheets (Fig. 1E), which was also demonstrated by AFM images, XPS spectra and zeta-potential analysis (Fig. S9, S10, and S11†). Since MnO₂ nanosheets had an intense and broadly optical absorption (Fig. S12†), the fluorescence of CpG-AgNCs was gradually quenched upon increasing the concentrations of MnO₂ nanosheets (Fig. 1F). Moreover, the quenching kinetics was fairly fast and needed only several tens of minutes (Fig. 1G). As tumors possess an acidic and H₂O₂-rich microenvironment, we proceeded to investigate the pH-/H₂O₂-responsive properties of MnO₂ nanosheets in a mimicking tumor microenvironment. As illustrated in Fig. 1H and S13,† under acidic H₂O₂ conditions, the quenched CpG-AgNCs fluorescence was recovered completely, which could be ascribed to the decomposition of MnO₂ nanosheets.

The loading and release of DOX on MnO₂-CpG-AgNCs (MCA) nanocomposites were studied. Owing to the strong electrostatic interaction and coordinate bonding between DOX and MnO₂ nanosheets, a high DOX-loading capacity was obtained. As illustrated in Fig. S14,† the loading capacity was as high as 70% when the DOX concentration was 0.5 mg mL⁻¹, much higher than the reported drug delivery systems. Thanks to the pH-/H₂O₂-responsive properties, MnO₂ nanosheets can be reduced into Mn²⁺ by acidic H₂O₂ in solid tumors, which could result in the release of DOX. Therefore, the release of DOX was monitored at pH values of 7.4, 6.0, and 4.5 in the presence of biologically relevant levels of H₂O₂, respectively. Nearly 90% of DOX was released at pH 4.5, whereas only 17% of DOX was detected at pH 7.4 (Fig. S15†). Collectively, it was demonstrated that the acidic H₂O₂ environment facilitated the dissociation of MnO₂ nanosheets and the subsequent release of DOX.

Investigation of ICD induced by DOX

Prior to studying the capacity of DOX to induce ICD, it is necessary to evaluate its cellular uptake in tumor cells. Compared with free DOX, substantially increased cell uptake of DOX was observed when using MnO₂ nanosheets as delivery systems, revealing that MnO₂ nanosheets could improve the cellular uptake of DOX and release it efficiently (Fig. S16†). Moreover, MnO₂-DOX exhibited enhanced cytotoxicity compared with the same amount of free DOX, validating that MnO₂ nanosheets were powerful nanocarriers for cancer treatment (Fig. S17–19†). Subsequently, we investigated the ICD-inducing capacity of DOX. Since a crucial step of ICD was the engulfment of dying tumor cells by professional macrophages, an *in vitro* phagocytosis analysis was performed.³³ The 4T1 tumor cells (pre-stained with CellTracker Orange) treated with

MnO₂-DOX were co-incubated with RAW 264.7 macrophages (CellTracker Green). Double-stained macrophages indicated that phagocytosis happened. As illustrated in Fig. 2A, both free DOX and MnO₂-DOX exhibited cytosolic mixing of the orange and green fluorescence in the contact region between 4T1 and RAW264.7 cells, showing that they were capable of promoting tumor-cell phagocytosis. Subsequently, three distinct biochemical hallmarks of ICD, namely CRT exposure, ATP secretion, and HMGB1 release, were determined. CRT acts as the dominant pro-phagocytic “eat me” signal and favors the phagocytosis to tumor antigen presentation, whereas ATP and HMGB1 as “find me” signals regulate DC-mediated tumor antigen cross-presentation and T-cell polarization.^{52,53} Flow cytometry results indicated that cells treated with DOX or MnO₂-DOX showed significant CRT expression on the cell surface, but none with PBS or MnO₂ nanosheets (Fig. 2B). The

immunostaining analysis was consistent with the flow cytometry results that cancer cells treated with MnO₂-DOX induced larger amounts of CRT expression than those treated with free DOX (Fig. 2C), which could be attributed to the enhanced cellular uptake and efficient release of MnO₂ nanocarriers. To evaluate ATP release in the cell supernatant, a conventional luciferase-based assay was conducted. As illustrated in Fig. 2D, the supernatant ATP content was significantly enhanced after DOX or MnO₂-DOX treatments compared with the control group. In addition to ATP secretion, the release of nuclear HMGB1 was also clearly apparent with DOX or MnO₂-DOX treatment, as determined by flow cytometry (Fig. 2E). Notably, MnO₂-DOX induced more ATP and HMGB1 release than free DOX, which was consistent with the results of CRT expression. Taken together, both DOX and MnO₂-DOX fulfilled all three molecular hallmarks of ICD, showing that our designed

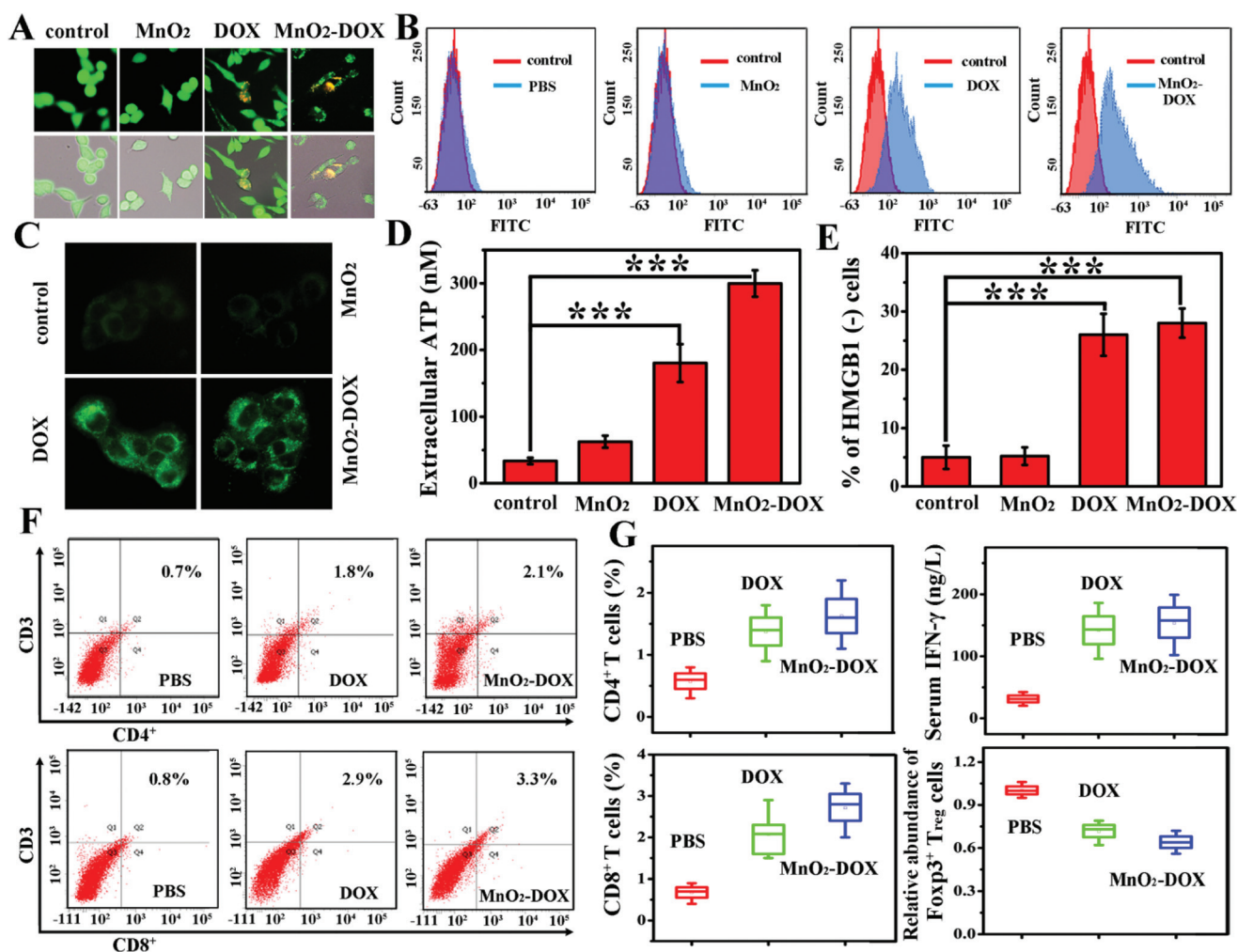


Fig. 2 (A) *In vitro* phagocytosis of MnO₂-DOX. Orange-stained 4T1 cells were treated with the indicated conditions before co-incubating with green-stained RAW264.7 cells. All images were obtained under a magnification of $\times 40$. (B) CRT exposure on the cell surface of 4T1 cells was evaluated after different treatments. (C) Immunofluorescence microscopy of CRT expression on the cell surface of 4T1 cells with different treatments. All images were acquired under a magnification of $\times 40$. (D) Extracellular release of ATP in 4T1 cells. (E) The release of nuclear HMGB1 from 4T1 cells after different treatments. Asterisks indicate statistically significant differences (* $P < 0.05$, ** $P < 0.01$, *** $P < 0.001$). (F) Quantification of T cells in tumors after various treatments indicated. (G) DOX and MnO₂-DOX treatment reversed T-cell suppression. Data are presented as the mean \pm standard errors of the mean.

system could act as an effective ICD inducer to initiate a robust immune response.

In vivo biological activity of DOX

To evaluate whether a DOX-based anticancer vaccine could engage a tumor-specific immune response *in vivo*, its biological activity was evaluated using 4T1 tumor-bearing mice as an animal model. As illustrated in Fig. 2G, mice treated with MnO₂-DOX or free DOX significantly increased the secretion of IFN- γ compared to the control group, indicating the efficient generation of immune response. Furthermore, the activation of antigen-specific CD8⁺ cytotoxic T lymphocytes (CTLs) and CD4⁺ T cells was also examined. It is clear that more CD4⁺ and CD8⁺ CTLs cells were found in the tumors treated with MnO₂-DOX (Fig. 2F). In addition to triggering a tumor-specific immune response, we also found that both MnO₂-DOX and DOX could alter immunosuppressive tumor microenvironments by abrogating the immune-suppressive activity of Tregs which hampered anti-tumor immune responses. As illustrated in Fig. 2G and Fig. S20,† the number of Tregs was significantly reduced and the ratios of CD8⁺ CTLs/Treg and CD4⁺ Teff/Treg were greatly increased in the tumors treated with MnO₂-DOX, indicating an effective strategy to surmount the immune escape mechanisms. Therefore, we envision that due to its unique merits, DOX could act as a promising immunomodulator to potentiate the immune effect of CpG ODNs.

Enhanced immune effect of MnO₂-CpG-AgNCs

With the exception of the immune effect of DOX, our well-designed nanocarrier may be another key factor for augmenting the immune response of CpG ODNs. It is worth noting that free CpG ODNs cannot reach their target sites. So far, various types of nanoparticle platforms including cationic lipids, polymers, gold nanoparticles, nanodiamonds *etc.* have been used to deliver CpG ODNs to stimulate immunological reactions in cells.^{7,54–56} Although promising, the interactions between CpG ODNs and the reported nanocarriers primarily relied on electrostatic or covalent interactions which are thermodynamically stable and inherently resistant to dissociation, inevitably decreasing the immune efficiency of CpG ODNs.^{57,58} In our strategy, MnO₂ nanosheets not only could protect CpG ODNs from nuclease degradation, but also release free CpG effectively and rapidly after reaching the destination. Such advantages would remarkably improve the immunostimulatory activity of CpG ODNs.

We then investigated the potential cytotoxicity of MCA nanocomposites on RAW264.7 cells by the conventional methyl thiazolyl tetrazolium (MTT) assay and the lactate dehydrogenase (LDH) assay. As illustrated in Fig. 3A and S21,† no clear cytotoxicity effect was detected for MCA nanocomposites, even on increasing the dosage of nanoparticles to 200 $\mu\text{g mL}^{-1}$, suggesting a good biocompatibility. To stimulate the immune response, the uptake of antigen-presenting cells to an exogenous adjuvant is critical for antigen presentation.⁵⁹ Fluorescence microscopy and flow cytometry were employed to

measure the cellular uptake efficiency. As shown in Fig. 3B, no apparent fluorescence was observed for cells treated with Rox-labeled CpG ODNs, which was likely due to the fact that naked CpG ODNs cannot pass the cytoplasmic membrane. Conversely, we detected a bright red fluorescence in cells incubated with CpG-AgNCs, clearly indicating that AgNCs could act as promising optical labels for tracking CpG.⁶⁰ In addition, much stronger red luminescence was observed in cells treated with MCA nanoparticles than those treated with CpG-AgNCs, clearly suggesting that MnO₂ nanosheets could improve the cellular uptake of CpG-AgNCs (Fig. 3B). Flow analysis also indicated that the cells incubated with MCA nanoparticles exhibited higher fluorescence intensity than those treated with CpG-AgNCs and free CpG (Fig. 3C), indicating that MnO₂ nanosheets were efficient delivery carriers for cancer therapy.

Having successfully substantiated the efficient cellular uptake of CpG-AgNCs, co-localization studies were conducted to track their internalization. After 4 h of incubation, both CpG-AgNCs and MCA nanoparticles were trapped in acidic lysosomes of RAW 264.7 cells, which could efficiently interact with TLR9 and induce the increased secretion of cytokines (Fig. 3D). IL-6, an inflammatory cytokine known to be up-regulated in macrophages following CpG stimulation, is a vital marker in the activation of humoral immunity.⁶¹ TNF- α , a pro-inflammatory cytokine mainly produced by macrophages, is one of the most important cytokines in cellular immunity.⁶² Accordingly, the levels of secreted inflammatory cytokines including IL-6 and TNF- α by RAW 264.7 cells with different treatments were measured by ELISA (Fig. 3E). Compared with free CpG or AgNP, CpG-AgNCs exhibited significantly higher immunostimulatory activity because of the enhanced cellular uptake. Notably, we found that the amount of TNF- α and IL-6 secretion caused by MCA was approximately twice as high as that of CpG-AgNCs. We speculated that the enhanced immunostimulatory effects were mainly mediated by the Mn²⁺ ions produced by the dissociation of MnO₂ nanosheets. As expected, MnO₂ nanosheets induced the clear secretion of IL-6 and TNF- α , which was in accordance with previous reports that Mn²⁺ ions were capable of activating macrophages and triggering the secretion of proinflammatory cytokines.⁶³ In addition to the adjuvant effect of Mn²⁺, the efficient release of CpG-AgNCs from MCA nanoparticles may be another key factor for this strong immune response. To identify our hypothesis, graphene oxide (GO) was introduced as the control since it has a sheeted structure like MnO₂ nanosheets but could not release CpG-AgNCs efficiently. As illustrated in Fig. 3E, the secretion of IL-6 and TNF- α caused by (GO-CpG-AgNCs minus GO) was diminished significantly compared to CpG-AgNCs owing to the inefficient CpG-AgNCs release. Therefore, using MnO₂ nanosheets to carry CpG-AgNCs was verified to be an attractive approach to improve their immunostimulatory activity.

Cell killing by synergistic effects

Inspired by the immunomodulatory capacity of DOX and the excellent immunostimulatory activity of MCA nanocomposites,

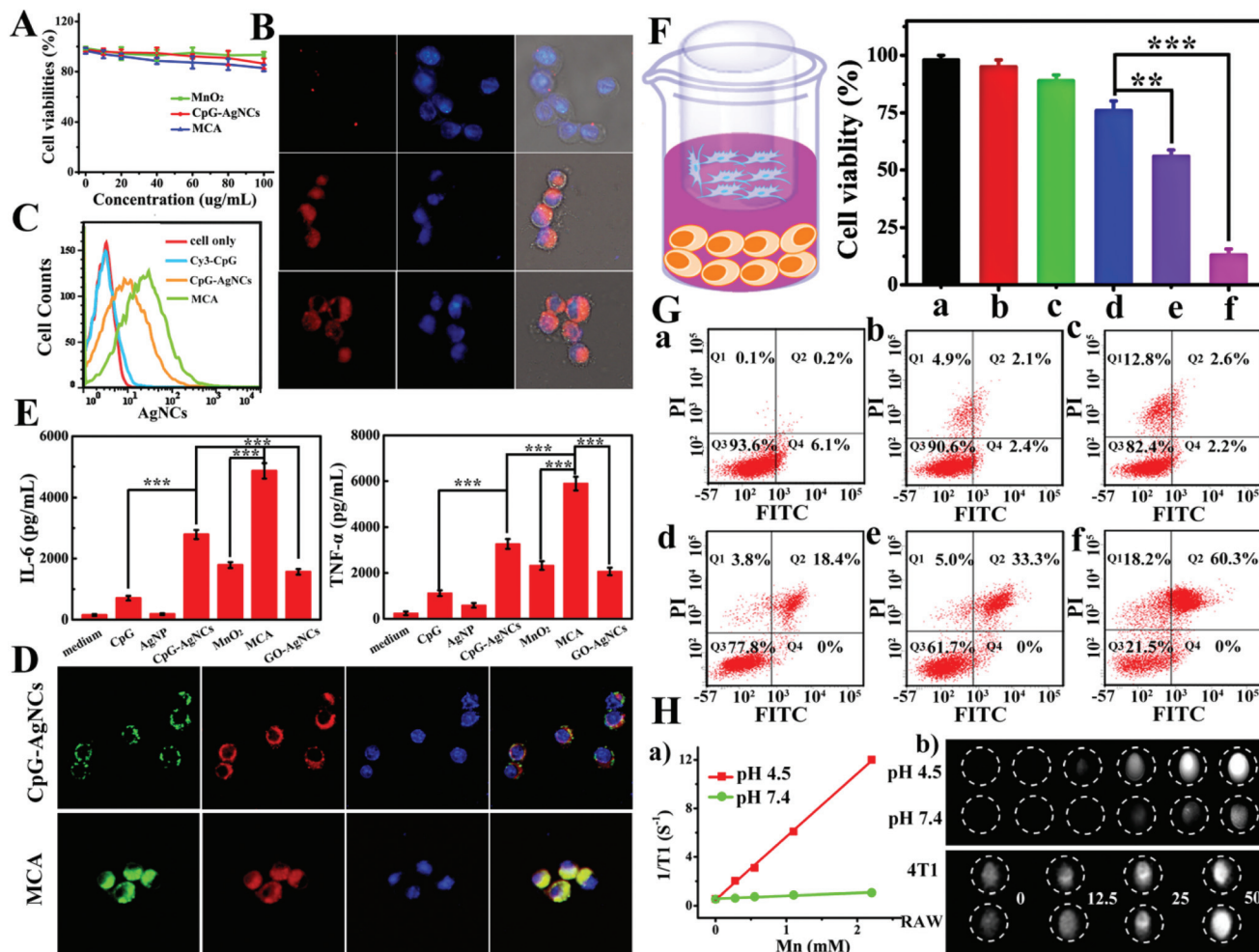


Fig. 3 MCA nanocomplexes triggered immunostimulation in macrophages. (A) The MTT assays of RAW264.7 cells treated with different groups. (B) Fluorescence microscopy of RAW264.7 cells treated with MCA nanocomplexes. The nuclei were stained with DAPI. All fluorescence images were acquired under a magnification of $\times 40$. (C) Cell uptake efficiency was assessed by flow cytometric analysis. (D) Fluorescence microscopy investigation of the localization of MCA nanocomplexes to RAW264.7 cells. The lysosomes were stained with Lyso-tracker Green. (E) Cytokine release from RAW264.7 cells stimulated by the different treatments. Error bars represent standard deviation of three independent measurements. (F) Schematic illustration of cell viability analysis in the 4T1 tumor cells (lower) and RAW264.7 cells (upper) co-culture system using Transwell plates. (a) Control; (b) MnO_2 nanosheets; (c) free CpG ODNs; (d) MCA nanocomplexes; (e) MnO_2 -DOX; (f) MCAD nanocomplexes. The values represent percentage cell viability (mean \pm SD, $n = 3$). Asterisks indicate statistically significant differences ($*P < 0.05$, $**P < 0.01$, $***P < 0.001$). (G) Flow cytometric analysis of 4T1 cell apoptosis induced by different formulations in a Transwell system. (a) Control; (b) MnO_2 nanosheets; (c) free CpG ODNs; (d) MCA nanocomplexes; (e) MnO_2 -DOX; (f) MCAD nanocomplexes. (H) Tumor microenvironment-responsive MRI of MCA nanocomplexes. (a) $\Delta 1/T_1$ versus M_n concentration for MCA solution in different values. (b) T_1 -Weight images of 4T1 cells and RAW264.7 cells treated with MCA nanocomplexes at different concentrations.

we next investigated whether the combination of DOX and MCA nanocomposites could lead to an enhanced therapeutic effect. To this end, using a Transwell system for mimicking the *in vivo* tumor model 4T1 cells were co-cultured with the RAW264.7 cells. As displayed in Fig. 3F, both MnO_2 nanosheets and free CpG exhibited a slight effect on the viability of 4T1 cells. In contrast, MCAD treatment offered the most effective cancer cell killing, which was higher than the therapeutic efficacy of both MCA and MnO_2 -DOX treatments. From the *t*-test analysis, a significant difference was observed between MCAD treatments and MCA/ MnO_2 -DOX treatments in inducing 4T1 cell death (Fig. 3F). Such results indicated that MCAD

could be an effective platform to inhibit tumor cell growth by triggering an enhanced immune response. Furthermore, the cell death mechanisms of 4T1 cells in the Transwell system were also evaluated by the typical fluorescein-annexin V and propidium iodide (PI) staining assay. As illustrated in Fig. 3G, MCAD induced cell toxicity was mainly associated with apoptosis, which was favorable for mediating an antitumor immune response. More importantly, quantitative analysis showed that the killing efficacy of MCAD was significantly higher than those of the sum of MnO_2 -DOX and MCA nanocomplexes, demonstrating the integration of DOX and CpG-AgNCs was able to enhance antitumor immunity.

Mn^{2+} ions produced by the decomposition of MnO_2 nanosheets had five unpaired 3d electrons and were considered excellent T_1 -weight agents in MR imaging.⁶⁴ Consequently, T_1 -weight MR imaging of MCA solutions after incubation in buffers with different pH values (4.5 and 7.4) for 2 h was performed. Compared with that in neutral buffer (pH 7.4), MCA nanocomposites dispersed in the acidic buffer showed a concentration-dependent brightening effect and the longitudinal relaxivity (r_1) value was also increased from $0.23 \text{ mM}^{-1} \text{ s}^{-1}$ at pH 7.4 to $5.2 \text{ mM}^{-1} \text{ s}^{-1}$ at pH 4.5. Besides, we also investigated the cell labelling ability of MCA nanocomposites. As illustrated in Fig. 3H, both RAW 264.7 cells and 4T1 cells exhibited enhanced magnetic resonance contrast with increasing concentrations of MCA nanocomposites. These results supported that our well-prepared MCA nanoparticles could be used as tumor-responsive MRI contrast agents.

In vivo antitumor activity of MCAD nanocomplexes

Finally, an antitumor study was performed to evaluate whether DOX could augment the immune response of CpG ODNs and improve their therapeutic effect *in vivo*. Considering the fact that local administration instead of system intravenous injection

is usually used for immunotherapy,⁶⁵ in our experiments, 4T1 tumor-bearing mice were intratumorally injected with PBS (control), MCA nanoparticles, MnO_2 -DOX and MCAD, respectively. After the tumor size reached about 100 mm^3 , the treatment efficacy was studied. As illustrated in Fig. 4A, MCA nanocomplexes failed to inhibit the growth of tumors. This result was in agreement with previous reports that CpG alone was incapable of acting against large solid tumors due to the pre-existing immune suppressive effect of the tumor environment.¹⁹ Although MnO_2 -DOX monotherapy led to clear tumor suppression in the early stages of treatment, it failed to inhibit tumor growth after 8 days, which might be attributed to the emergence of drug resistance. Comparatively, with the assistance of DOX, CpG exhibited admirable antitumor immunity so that the growth of tumors was almost completely inhibited (Fig. 4A). The tumor mass from each group was removed and weighed to calculate the tumor inhibition rate. As shown in Fig. 4C, the MCAD group exhibited remarkable antitumor activity against large solid tumors compared to MCA treatment. Moreover, MCAD treatment resulted in a 95% inhibition rate on tumor growth, which was 3.9-fold higher than that of MCA therapy ($p < 0.05$), as shown in Fig. 4D. Furthermore,

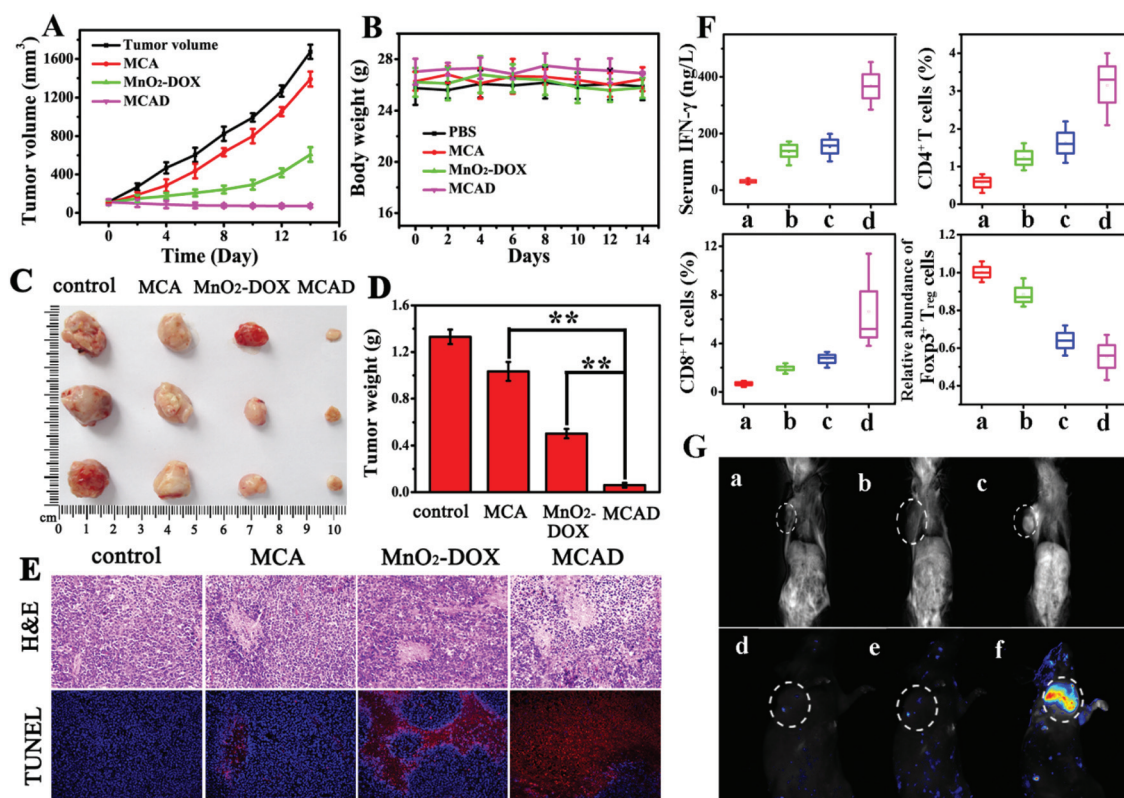


Fig. 4 *In vivo* antitumour activity of MCAD nanocomposites. (A) Tumour growth curves of different groups of mice (5 mice per group). (B) Changes with time in body weight obtained from mice treated with PBS, MCA, MnO_2 -DOX and MCAD nanocomposites. (C) Representative images of the tumours at the 14th day. (D) Tumour weights of different groups at the 14th day. Asterisks indicate statistically significant differences ($*P < 0.05$, $**P < 0.01$, $***P < 0.001$). (E) H&E staining and TUNEL staining of tumour tissues at the 14th day. Nuclei were stained blue (DAPI staining, $\times 20$), and apoptotic cells were stained red (TUNEL staining, $\times 20$). (F) Tumour-specific immune responses. (G) *In vivo* T_1 -weight MR images of tumour bearing mice taken (a) before injection, (b) 5 min, and (c) 24 h post injection of MCA nanocomposites. Fluorescence images of tumour bearing mice taken (d) before injection, (e) 5 min, and (f) 24 h post injection of MCA nanocomplexes.

images of hematoxylin and eosin (H&E) and terminal deoxynucleotidyl transferase dUTP nick-end labeling (TUNEL) stained tumor slices further confirmed that after MCAD treatment the tumor cells were severely destroyed, showing remarkably greater therapeutic efficacy than that of single chemotherapy or immunotherapy (Fig. 4E). These results indicated that the proportion of cancer cells responding to CpG ODN-mediated immunotherapy was substantially increased by combining DOX. Besides, we also evaluated the systemic toxicity of our nanoplatform. As illustrated in Fig. 4B, no significant change in body weight over the course of the treatments was observed. Moreover, there was no noticeable tissue damage or adverse effects on major organs (Fig. S22 and 23[†]), reflecting the good biocompatibility of our system *in vivo*.

The immunological mechanisms of MCAD nanocomplexes *in vivo*

To investigate the immunological mechanisms behind the outstanding therapeutic effects of our formulation, tumor-infiltrating lymphocytes from relapsed tumors were harvested and analyzed by flow cytometry. It is well known that CTL ($CD3^+ CD8^+$) could directly kill tumor cells and helper T cells ($CD3^+ CD4^+$) played crucial roles in regulating adaptive immunity.⁶⁶ The MCDA nanocomposites not only increased $CD4^+$ T cell proliferation, but also significantly heightened the tumor infiltration of $CD8^+$ T cells (Fig. 4F), suggesting that MCAD nanocomposites were an effective immunomodulatory agent. Besides, the tumor-infiltrating $CD4^+$ FoxP3⁺ T cells were also studied. As illustrated in Fig. S24,[†] both the ratios of $CD8^+$ T cells to Tregs and $CD4^+$ T cells to Tregs were remarkably improved after MCAD treatment, which were important for improving the anti-tumor immunological response. In contrast, for MCA nanocomplexes, most of the increased $CD4^+$ T cells were found to be Tregs, resulting in the ineffectiveness of anti-tumor immune responses. Therefore, we concluded that the efficient immune response of CpG-AgNCs was attributed to the immune modulation capacity of DOX, which reversed the immunosuppressive microenvironments of tumors and induced ICD successfully. Further analysis of the secretion of cytokine in serum was performed. IFN- γ is a pleiotropic cytokine and plays an important role in the innate immune response to tumors, including the activation of mononuclear phagocytes and promoting the differentiation of CTLs from $CD8$ T cell precursors.⁶⁷ IFN- γ is mainly secreted by the Th1 subset of $CD4^+$ T cells and $CD8^+$ CTLs, whereas Th1 type immune responses are imperative to trigger immune responses, which is of great importance to treat cancers.⁶⁸ Therefore, the concentration of IFN- γ was measured at 3 days post-injection to evaluate the generation of cytokines caused by MCAD nanocomposites *in vivo*. We found that the levels of IFN- γ in serum treatment with MCAD nanocomposites was nearly 2 fold more than that of MCA or MnO_2 -DOX alone. These results suggested that the antitumor immunity of CpG-AgNCs was significantly enhanced by the DOX-caused tumor-specific immune response.

Tumor-activatable MRI and fluorescence imaging

Encouraged by the above *in vivo* therapy results, we further investigated whether such a pH-/H₂O₂-responsive nanotherapeutic was suitable for *in vivo* tumor imaging. The T_1 -weighted MRI was conducted on 4T1 tumor-bearing mice at different time points post intratumoral injection of MCA (5 mg kg⁻¹), and the resulting images are shown in Fig. 4G. No significant MRI contrast showed up at 5 min post injection, whereas a marked positive enhancement was detected at 24 h post injection. The significant tumor contrast was therefore a result of gradual degradation of MnO_2 nanosheets in acidic H₂O₂ tumor microenvironments. Along with MR imaging, our MCA nanoplatform could also provide tumor-activatable fluorescence imaging to the tumor-bearing mice. Corresponding to the results of MRI, no clear signal was observed at 5 min post-injection (Fig. 4G). Comparatively, the tumor signal increased and could be easily differentiated from the surrounding normal tissue with good contrast 24 h post injection. These results indicated that MCA nanocomposites possessed excellent MRI and fluorescence imaging ability and were able to real-time track CpG-AgNCs release or depict tumors.

Conclusions

In conclusion, for the first time, we have demonstrated that common chemotherapy drug DOX could serve as a bifunctional modulator to boost CpG ODN-mediated immunotherapy by inducing ICD and decreasing the immunosuppressive mechanism of the tumor microenvironment. In our design, MnO_2 nanosheets were chosen as nanocarriers to co-deliver DOX and CpG-AgNCs because of their appealing pH-/redox-responsive properties, abundant anchoring points, as well as extremely large surface area. DOX could serve as a workable ICD to activate an innate and adaptive immune response, which was demonstrated by three distinct biochemical hallmarks of ICD, namely CRT exposure, ATP excretion and HGMB1 release. More importantly, *in vivo* experiments have demonstrated that DOX was able to abrogate the immune-suppressive activity of Tregs and improve the activities of $CD8^+$ T cells. Such a bifunctional immunoregulation capacity of DOX greatly enhanced the therapeutic effect of CpG-mediated immunotherapy. As a result, the MCAD nanocomposites not only created an immunogenic tumor environment but also exhibited the excellent antitumor effect for large solid tumors. Additionally, *in vivo* experiments have demonstrated that our MCA nanocomposites could act as effective contrast agents for dual-mode MRI and fluorescence imaging, enabling us to better track the involved physiological and pathological process in the region of interest as well as analyze the treatment efficacy. Taken together, we believe that our work could pave the way for applying clinically used chemotherapy drugs with an immunomodulation capacity to boost cancer immunotherapy.

Conflicts of interest

There are no conflicts to declare.

Acknowledgements

The authors are grateful to the referee for helpful comments on the manuscript. Financial support was provided by the National Natural Science Foundation of China (grant no. 2121002, 21431007, 21403209, and 21533008).

Notes and references

- R. Kuai, L. J. Ochyl, K. S. Bahjat, A. Schwendeman and J. J. Moon, *Nat. Mater.*, 2016, **16**, 489.
- H. Liu, K. D. Moynihan, Y. Zheng, G. L. Szeto, A. V. Li, B. Huang, D. S. Van Egeren, C. Park and D. J. Irvine, *Nature*, 2014, **507**, 519.
- G. J. Weiner, H.-M. Liu, J. E. Wooldridge, C. E. Dahle and A. M. Krieg, *Proc. Natl. Acad. Sci. U. S. A.*, 1997, **94**, 10833.
- A. M. Krieg, A.-K. Yi, S. Matson, T. J. Waldschmidt, G. A. Bishop, R. Teasdale, G. A. Koretzky and D. M. Klinman, *Nature*, 1995, **374**, 546.
- J. Vollmer and A. M. Krieg, *Adv. Drug Delivery Rev.*, 2009, **61**, 195.
- M. Wei, N. Chen, J. Li, M. Yin, L. Liang, Y. He, H. Song, C. Fan and Q. Huang, *Angew. Chem., Int. Ed.*, 2012, **51**, 1202.
- Y. Zhang, Z. Cui, H. Kong, K. Xia, L. Pan, J. Li, Y. Sun, J. Shi, L. Wang, Y. Zhu and C. Fan, *Adv. Mater.*, 2016, **28**, 299.
- B. Badie and J. M. Berlin, *Immunotherapy*, 2012, **5**, 1.
- A. Carpentier, F. Laigle-Donadey, S. Zohar, L. Capelle, A. Behin, A. Tibi, N. Martin-Duverneuil, M. Sanson, L. Lacomblez, S. Taillibert, L. Puybasset, R. Van Effenterre, J.-Y. Delattre and A. F. Carpentier, *J. Neuro-Oncol.*, 2006, **8**, 60.
- S. de Jong, G. Chikh, L. Sekirov, S. Raney, S. Semple, S. Klimuk, N. Yuan, M. Hope, P. Cullis and Y. Tam, *Cancer Immunol. Immunother.*, 2007, **56**, 1251.
- J. S. Weber, H. Zarour, B. Redman, U. Trefzer, S. O'Day, A. J. M. van den Eertwegh, E. Marshall and S. Wagner, *Cancer*, 2009, **115**, 3944.
- H. Zheng, S. Wen, Y. Zhang and Z. Sun, *PLoS One*, 2015, **10**, e0140265.
- A. de Titta, M. Ballester, Z. Julier, C. Nembrini, L. Jeanbart, A. J. van der Vlies, M. A. Swartz and J. A. Hubbell, *Proc. Natl. Acad. Sci. U. S. A.*, 2013, **110**, 19902.
- Y. C. Song, H. Y. Cheng, C. H. Leng, S. K. Chiang, C. W. Lin, P. Chong, M. H. Huang and S. J. Liu, *J. Controlled Release*, 2014, **173**, 158.
- J. A. Joyce and D. T. Fearon, *Science*, 2015, **348**, 74.
- H. Liu, B. Kwong and D. J. Irvine, *Angew. Chem., Int. Ed.*, 2011, **50**, 7052.
- A. Y. Lin, J. P. Almeida, A. Bear, N. Liu, L. Luo, A. E. Foster and R. A. Drezek, *PLoS One*, 2013, **8**, e63550.
- C. He, X. Duan, N. Guo, C. Chan, C. Poon, R. R. Weichselbaum and W. Lin, *Nat. Commun.*, 2016, **7**, 12499.
- A. M. Krieg, *Curr. Oncol. Rep.*, 2004, **6**, 88.
- C. Wang, W. Sun, G. Wright, A. Z. Wang and Z. Gu, *Adv. Mater.*, 2016, **28**, 8912.
- L. Guo, D. D. Yan, D. Yang, Y. Li, X. Wang, O. Zalewski, B. Yan and W. Lu, *ACS Nano*, 2014, **8**, 5670.
- A. Q. Butt and K. H. G. Mills, *Oncogene*, 2014, **33**, 4623.
- S. M. Mangsbo, L. C. Sandin, K. Anger, A. J. Korman, A. Loskog and T. H. Tötterman, *J. Immunother.*, 2010, **33**, 225.
- P. Sharma and J. P. Allison, *Cell*, 2015, **161**, 205.
- Q. Chen, L. Xu, C. Liang, C. Wang, R. Peng and Z. Liu, *Nat. Commun.*, 2016, **7**, 13193.
- L. Gelao, C. Criscitiello, A. Esposito, A. Goldhirsch and G. Curigliano, *Toxins*, 2014, **6**, 914.
- C. Wang, Y. Ye, G. M. Hochu, H. Sadeghifar and Z. Gu, *Nano Lett.*, 2016, **16**, 2334.
- Y. Chen, R. Xia, Y. Huang, W. Zhao, J. Li, X. Zhang, P. Wang, R. Venkataramanan, J. Fan, W. Xie, X. Ma, B. Lu and S. Li, *Nat. Commun.*, 2016, **7**, 13443.
- R. A. Lake and B. W. S. Robinson, *Nat. Rev. Cancer*, 2005, **5**, 397.
- L. A. Emens and G. Middleton, *Cancer Immunol. Res.*, 2015, **3**, 436.
- A. G. Dalgleish, *Immunotherapy*, 2015, **7**, 309.
- A. Tesniere, F. Schlemmer, V. Boige, O. Kepp, I. Martins, F. Ghiringhelli, L. Aymeric, M. Michaud, L. Apetoh, L. Barault, J. Mendiboure, J. P. Pignon, V. Jooste, P. van Endert, M. Ducreux, L. Zitvogel, F. Piard and G. Kroemer, *Oncogene*, 2010, **29**, 482.
- D. Y. Q. Wong, W. W. F. Ong and W. H. Ang, *Angew. Chem., Int. Ed.*, 2015, **54**, 6483.
- J. J. Luke and G. K. Schwartz, *Clin. Dermatol.*, 2013, **31**, 290.
- C. G. Drake, E. J. Lipson and J. R. Brahmer, *Nat. Rev. Clin. Oncol.*, 2014, **11**, 24.
- M. H. Kershaw, C. Devaud, L. B. John, J. A. Westwood and P. K. Darcy, *OncoImmunology*, 2013, **2**, e25962.
- D. W. Zheng, J. L. Chen, J. Y. Zhu, L. Rong, B. Li, Q. Lei, J. X. Fan, M. Z. Zou, C. Li, S. X. Cheng, Z. Xu and X. Z. Zhang, *Nano Lett.*, 2016, **16**, 4341.
- N. Casares, M. O. Pequignot, A. Tesniere, F. Ghiringhelli, S. Roux, N. Chaput, E. Schmitt, A. Hamai, S. Hervas-Stubbs, M. Obeid, F. Coutant, D. Metivier, E. Pichard, P. Aucoeur, G. Pierron, C. Garrido, L. Zitvogel and G. Kroemer, *J. Exp. Med.*, 2005, **202**, 1691.
- E. Proietti, F. Moschella, I. Capone and F. Belardelli, *Mol. Oncol.*, 2012, **6**, 1.
- R. Ramakrishnan and D. I. Gabrilovich, *Cancer Immunol. Immunother.*, 2013, **62**, 405.
- J. Ren, L. Di, G. Song, J. Yu, J. Jia, Y. Zhu, Y. Yan, H. Jiang, X. Liang, L. Che, J. Zhang, F. Wan, X. Wang, X. Zhou and H. K. Lyerly, *Clin. Transl. Oncol.*, 2013, **15**, 780.

- 42 A. Tesniere, T. Panaretakis, O. Kepp, L. Apetoh, F. Ghiringhelli, L. Zitvogel and G. Kroemer, *Cell Death Differ.*, 2008, **15**, 3.
- 43 H. Wildiers, R. Jurcut, J. Ganame, L. Herbots, P. Neven, J. De Backer, H. Denys, V. Cocquyt, F. Rademakers, J.-U. Voigt and R. Paridaens, *Crit. Rev. Oncol. Hematol.*, 2008, **67**, 133.
- 44 A. Marabelle, H. Kohrt, I. Sagiv-Barfi, B. Ajami, R. C. Axtell, G. Zhou, R. Rajapaksa, M. R. Green, J. Torchia, J. Brody, R. Luong, M. D. Rosenblum, L. Steinman, H. I. Levitsky, V. Tse and R. Levy, *J. Clin. Invest.*, 2013, **123**, 2447.
- 45 D. Alizadeh, M. Trad, N. T. Hanke, C. B. Larmonier, N. Janikashvili, B. Bonnotte, E. Katsanis and N. Larmonier, *Cancer Res.*, 2014, **74**, 104.
- 46 M. Tongu, N. Harashima, T. Yamada, T. Harada and M. Harada, *Cancer Immunol. Immunother.*, 2010, **59**, 769.
- 47 T. Ghansah, N. Vohra, K. Kinney, A. Weber, K. Kodumudi, G. Springett, A. A. Sarnaik and S. Pilon-Thomas, *Cancer Immunol. Immunother.*, 2013, **62**, 1083.
- 48 Z. G. Fridlender, J. Sun, S. Singhal, V. Kapoor, G. Cheng, E. Suzuki and S. M. Aleida, *Mol. Ther.*, 2010, **18**, 1947.
- 49 Z. Zhao, H. Fan, G. Zhou, H. Bai, H. Liang, R. Wang, X. Zhang and W. Tan, *J. Am. Chem. Soc.*, 2014, **136**, 11220.
- 50 Y. Tao, E. Ju, Z. Li, J. Ren and X. Qu, *Adv. Funct. Mater.*, 2014, **24**, 1004.
- 51 Y. Chen, D. Ye, M. Wu, H. Chen, L. Zhang, J. Shi and L. Wang, *Adv. Mater.*, 2014, **26**, 7019.
- 52 R. Deng, X. Xie, M. Vendrell, Y. T. Chang and X. Liu, *J. Am. Chem. Soc.*, 2011, **133**, 20168.
- 53 L. Bracci, G. Schiavoni, A. Sistigu and F. Belardelli, *Cell Death Differ.*, 2014, **21**, 15.
- 54 M. Obeid, A. Tesniere, F. Ghiringhelli, G. M. Fimia, L. Apetoh, J. L. Perfettini, M. Castedo, G. Mignot, T. Panaretakis, N. Casares, D. Metivier, N. Larochette, P. van Endert, F. Ciccocanti, M. Piacentini, L. Zitvogel and G. Kroemer, *Nat. Med.*, 2007, **13**, 54.
- 55 S.-Y. Kim, M. B. Heo, G.-S. Hwang, Y. Jung, D. Y. Choi, Y.-M. Park and Y. T. Lim, *Angew. Chem., Int. Ed.*, 2015, **54**, 8139.
- 56 A. Bianco, J. Hoebeke, S. Godefroy, O. Chaloin, D. Pantarotto, J.-P. Briand, S. Muller, M. Prato and C. D. Partidos, *J. Am. Chem. Soc.*, 2005, **127**, 58.
- 57 J. P. M. Almeida, A. Y. Lin, E. R. Foster, E. R. Figueroa, A. E. Foster and R. A. Drezek, *Small*, 2015, **11**, 1453.
- 58 Z. Li, Y. Tao, S. Huang, N. Gao, J. Ren and X. Qu, *Chem. Commun.*, 2013, **49**, 7129.
- 59 I. H. Lee, H. K. Kwon, S. An, D. Kim, S. Kim, M. K. Yu, J. H. Lee, T. S. Lee, S. H. Im and S. Jon, *Angew. Chem., Int. Ed.*, 2012, **51**, 8800.
- 60 Y. Zhang, F. Wang, E. Ju, Z. Liu, Z. Chen, J. Ren and X. Qu, *Adv. Funct. Mater.*, 2016, **26**, 6454.
- 61 L. Bracci, G. Schiavoni, A. Sistigu and F. Belardelli, *Cell Death Differ.*, 2014, **21**, 15.
- 62 M. Nishikawa, Y. Mizuno, K. Mohri, N. Matsuoka, S. Rattanakit, Y. Takahashi, H. Funabashi, D. Luo and Y. Takakura, *Biomaterials*, 2011, **32**, 488.
- 63 Y. Tao, M. Li, J. Ren and X. Qu, *Chem. Soc. Rev.*, 2015, **44**, 8636.
- 64 R. J. Smialowicz, R. R. Rogers, M. M. Riddle, R. W. Luebke, L. D. Fogelson and D. G. Rowe, *J. Toxicol. Environ. Health*, 1987, **20**, 67.
- 65 Y. Kwarada, R. Ganss, N. Garbi, T. Sacher, B. Arnold and G. J. Hammerling, *J. Immunol.*, 2001, **167**, 5247.
- 66 D. Wang, T. Wang, J. Liu, H. Yu, S. Jiao, B. Feng, F. Zhou, Y. Fu, Q. Yin, P. Zhang, Z. Zhang, Z. Zhou and Y. Li, *Nano Lett.*, 2016, **16**, 5503.
- 67 Z. Moldoveanu, L. Love-Homan, W. Q. Huang and A. M. Krieg, *Vaccine*, 1988, **16**, 11.
- 68 Y. H. Cao, Y. F. Ma, M. X. Zhang, H. M. Wang, X. L. Tu, H. Shen, J. W. Dai, H. C. Guo and Z. J. Zhang, *Adv. Funct. Mater.*, 2014, **24**, 6963.